Chapter 2
Ambient-Pressure X-ray Photoelectron Spectroscopy (APXPS)

Osman Karslıoğlu and Hendrik Bluhm

Abstract X-ray photoelectron spectroscopy (XPS) is a powerful technique for studying surfaces, including those of heterogeneous catalysts, through its ability to quantitatively analyze the elemental and chemical composition with high surface sensitivity. The understanding of heterogeneous catalytic processes under realistic conditions requires measurements at elevated pressures, far from the high-vacuum conditions under which the majority of XPS measurements are conducted. The investigation of surfaces using XPS at or near relevant pressures poses challenges due to scattering of electrons by gas molecules, which have been overcome through the development of ambient-pressure XPS (APXPS). In this chapter, we will review technical approaches for conducting XPS at higher pressures and discuss other experimental challenges that need to be addressed in APXPS investigations. At the end of the chapter, examples of APXPS experiments of CO oxidation over Ru and Pd, as well as the oxidation of other small hydrocarbons are shown.

2.1 Technique

2.1.1 Basics of XPS

XPS is a surface-sensitive chemical-analysis technique, which has become a common tool in laboratories all around the world. Its applications span a wide range of fields from catalysis to electronics. The technique relies on the distinct binding energies of core electrons in different elements. Qualitatively, binding energy is a measure of how tightly an electron is bound to an atom. From a fundamental perspective, one can start defining it by considering the photoemission process. For an isolated atom, energy conservation during photoemission can be expressed as:

O. Karslıoğlu · H. Bluhm (✉)
Lawrence Berkeley National Laboratory, Chemical Sciences Division,
1 Cyclotron Road, Berkeley, CA 94720, USA
e-mail: hbluhm@lbl.gov

$$E_i^N + h\nu = E_f^{N-1} + E_{kin} \tag{2.1}$$

where $h\nu$ is the photon energy, E_{kin} is the kinetic energy of the photoelectron, and E_i and E_f are the initial (N particles) and final (N − 1 particles) energies of the system. After rearranging the terms and defining:

$$E_b \equiv E_f^{N-1} - E_i^N \tag{2.2}$$

the equation becomes:

$$E_b = h\nu - E_{kin} \tag{2.3}$$

where E_b is the binding energy of an electron in the atom. Equation 2.3 implies that the binding energy is referenced to vacuum (free electron at rest). For solids (condensed phases in general) it is customary to define the binding energy relative to the Fermi level, which serves as a more practical reference. For solids, 2.3 is modified to:

$$E_b = h\nu - E_{kin} - \phi \tag{2.4}$$

where ϕ is the work function of the surface wherever E_{kin} is measured at, in the case of XPS that of the electron analyzer. The equation holds only if the Fermi levels of the sample and analyzer are aligned, which is the default configuration.

The binding energy of an electron depends mainly on the type of atom that it is bound to and its quantum state (i.e. energy level, 1s, 2s, 2p, etc.). In addition, differences in the chemical environment of an element (i.e. its oxidation state) can also cause changes in binding energy. These changes are referred to as chemical shifts, and it is the power to resolve these subtle differences that makes XPS an excellent method for the investigation of surface chemistry.

In an XPS experiment, monochromatic X-rays irradiate the sample and excite electrons in a sample to unbound states (i.e. to vacuum) and the number of electrons is counted as a function of kinetic energy. The kinetic-energy axis is usually converted to binding energy using 2.4. Most X-ray photoelectron spectrometers are of the concentric hemispherical-analyzer type, where the photoelectrons that leave the sample are collected by an electrostatic lens system, which focuses the electrons onto the entrance aperture of the concentric hemispherical analyzer. The heart of the electron-energy analyzer consists of two concentric hemispheres, which are biased such that only electrons with a certain kinetic energy (i.e. "pass energy") reach the electron detector (e.g. channeltrons or a phosphor screen with camera), which is situated at the exit of the hemispherical analyzer.

2.1.2 Operating XPS at Elevated Pressure

There are two basic problems that need to be overcome in XPS experiments under non-vacuum conditions. The fundamental problem is the scattering of photoelectrons by gas molecules, which limits the distance that electrons can travel through the gas atmosphere. For instance, the inelastic mean free path (IMFP) of electrons in water vapor at 1 Torr for 100 eV kinetic-energy electrons is about 1 mm, much shorter than the path length of electrons in a spectrometer, which is typically on the order of a meter or more. The other issue is of technical nature and concerns discharging through the gas where high voltage differences are present, as in the electrostatic lens system or the electron detectors. The voltages applied to the lens elements in general increase with the kinetic energy of the electrons analyzed and at some point a critical electrical-field gradient between adjacent lens elements is reached which leads to a gas discharge. This problem can be addressed through the appropriate design of the electrostatic lens (e.g. large enough gaps between the lens elements), the use of lens tables that avoid large potential differences between adjacent lens elements, as well as efficient differential pumping. In the following we will address some of the design criteria for ambient-pressure photoelectron spectrometers.

2.1.2.1 Electron Scattering in Matter

Electrons are scattered very strongly in matter due to the nature of electron-electron interactions [1]. For electrons with kinetic energies (E_{kin}) below the ionization energy of the gas molecules (typically below 10 eV), the nature of the interaction is elastic, which means electrons change direction but do not lose energy. The effect of elastic scattering to signal attenuation depends on the experimental configuration. If the area of the sample illuminated by the X-rays is large compared to the area seen by the spectrometer, the effect will be small—electrons scattered out of the acceptance cone will be compensated by the electrons scattered into it. If the X-ray spot is small, this compensation will not happen and more signal will be lost. In any case, the effect of elastic scattering will be small in a typical APXPS experiment since scattering is predominantly in the forward direction, and most APXPS experiments detect photoelectrons with higher kinetic energies, where elastic scattering is less relevant.

For kinetic energies above the ionization energy threshold, electron-molecule collisions may result in energy loss for the electron, i.e. inelastic scattering. This is the principal signal-attenuation mechanism in APXPS. Electrons with kinetic energies around 50–100 eV are scattered most strongly and thus have the smallest IMFP. The electron scattering cross section decreases as E_{kin} increases beyond 100 eV. For a more detailed discussion of different scattering mechanisms, the reader may refer to [2].

Signal attenuation due to electron scattering in the gas becomes a problem when the signal-to-noise ratio becomes too small for the acquisition of a spectrum to be completed within a "reasonable" period of time. For electrons with a given kinetic energy the acquisition time depends not only on the gas pressure and the electrons' path length in the gas but also on other factors. The signal is proportional to the photon flux and the photoionization cross section of the investigated core level, whereas the signal-to-noise ratio decreases with the peak-width of the core level and the electron scattering cross section of the gas molecule. It also depends on the acquisition parameters of the analyzer such as the pass energy.

Assuming all other parameters (e.g. photon flux, analyzer transmission, etc.) are kept constant, one can estimate a practical maximum pressure based on a typical distance that electrons can travel in a gas and the distance between the sample and the differentially-pumped entrance aperture to the spectrometer lens. The inelastic mean free path in condensed matter for electrons with 100 eV kinetic energy is about a nanometer [3]. Gases are about 1000 times less dense than their condensed forms at atmospheric conditions. This means electrons with ∼100 eV kinetic energy can travel around 1 μm in a gas at 1 atm, which would limit the entrance aperture size to the same order of magnitude to avoid pressure inhomogeneities at the sample surface (see below) and also requires a tightly-focused X-ray beam that impinges on the sample surface under a very shallow angle to avoid shadowing by the aperture. More practical aperture-sample distances are in the 100 μm range, but this leads to a pressure limit of ∼2 orders of magnitude lower than 1 atm. This means that most APXPS experiments currently are carried out at pressures below 10 Torr and at sample—aperture distances of 0.1 to 1 mm.

The electrostatic lens needs to be at a low enough pressure for the electrons to travel without significant scattering, and the electron detector needs to be at pressures well below 10^{-6} Torr. Transitioning from a high-pressure region to a low-pressure region can be done in two ways. One is to introduce a gas-impermeable but electron-permeable membrane between the sample and the spectrometer, such as graphene. This provides an abrupt drop in pressure, from Torr range to ultrahigh vacuum (UHV), and would be an ideal solution in terms of reducing the size and cost of the spectrometer (see Fig. 2.1b). However, this approach has so far shown to be difficult to implement technically due to the stringent requirements on the mechanical stability of the ultrathin membranes. Nevertheless, there are ongoing efforts in this direction [4–7], which recently resulted in successful demonstrations at 1 bar pressure [8, 9]. In the following we will focus on the most-commonly used scheme to transition from the ambient pressures in the sample compartment to high vacuum in the electron detector, namely the use of differential pumping [10].

2.1.2.2 Separation of Sample Cell and Electron Spectrometer by Differential Pumping

The conventional solution to reducing the path length of electrons through the gas phase in the sample cell has been to decrease the pressure using differential-pumping

(a)   Practical solution – Multiple differential pumping stages

$p_1 \ll p_0$ $p_2 \ll p_1$ $< 10^{-7}$ Torr

p_0

$p_0^{max} \approx 10$ Torr
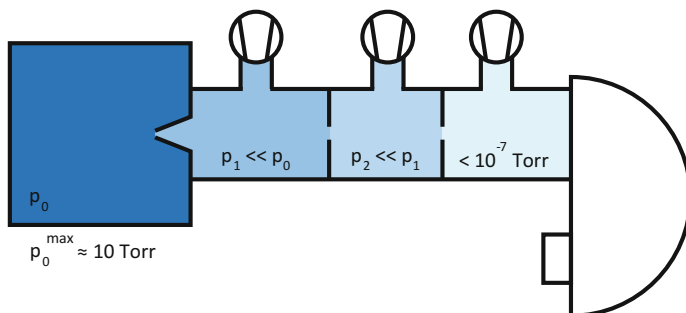
(b)   Ideal solution – Electron-permeable ultrathin membrane


$< 10^{-7}$ Torr

p_0
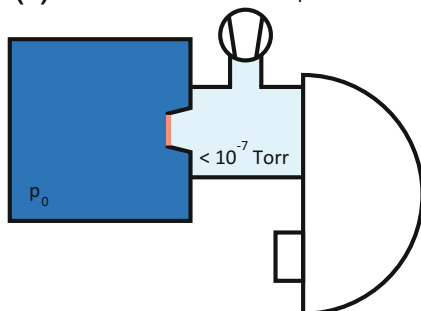
Fig. 2.1 Two possible schemes for an APXPS setup to transition from a high pressure at the sample to UHV at the electron detector. **a** Decreasing the pressure gradually using multiple differential pumping stages, **b** decreasing the pressure abruptly using an ultrathin membrane, which is permeable to electrons but impermeable to molecules

stages along the electron path. The differential-pumping stages are usually separated by apertures of the size on the order of a few millimeter, with the first aperture (facing the sample) of sub-millimeter dimensions. The apertures are small enough to limit gas flow but large enough to allow electron transmission. Figure 2.1a shows schematically how such a differential-pumping system works.

The differential-pumping system creates a pressure gradient along the electron trajectory. Molecular-flow equations for an aperture with negligible length indicate that most of the pressure drop occurs within two diameter-lengths around the aperture on the spectrometer axis. Figure 2.2a shows a sample placed at a distance "z" from the aperture, which has a radius of R. The calculated pressure map is plotted in part (b) of the figure. The details of the calculation can be found in [11]. Distances are given in units of R. The expression for pressure on the z-axis is:

Fig. 2.2 Pressure near an aperture, which is differentially pumped on the right side. The pressure on the differentially-pumped side, sufficiently far away from the aperture, is much smaller than p_0, the pressure on the high-pressure side far away from the aperture. **a** Sample placed at a distance z from the plane of an aperture with radius R. **b** Isobars in the y-z plane. Pressures are in units of p_0 and coordinates are in units of R. Reproduced with permission from [12]
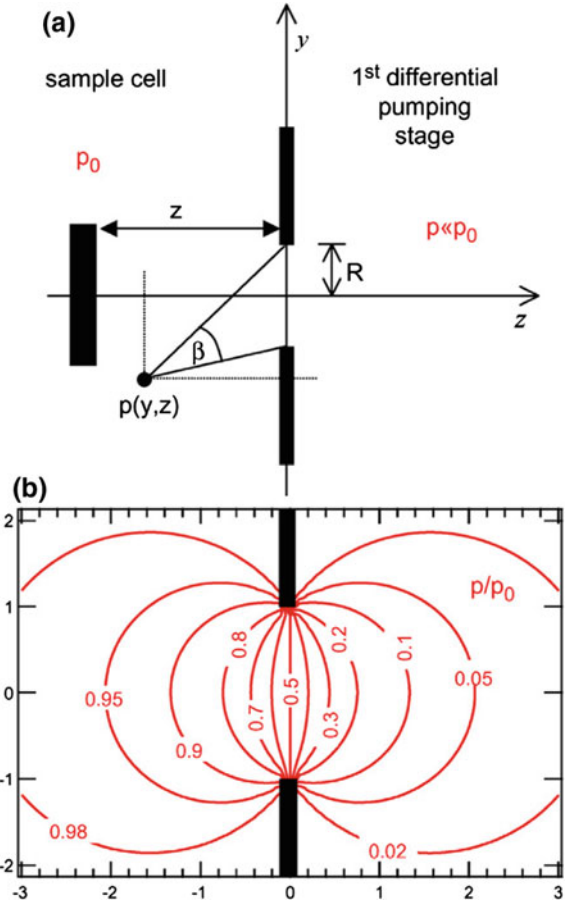
$$p(z) = \frac{1}{2}p_0\left(1 - \frac{z}{\sqrt{1+z^2}}\right) \tag{2.5}$$

This means that the electrons experience different pressures at different points along the path to the analyzer. For a simplified view one can assume that the electrons experience a pressure of p_0 for a shorter path length, which we define as "effective length", and experience no gas pressure for the rest of the path. Effective length L for electrons emerging from point $(y = 0, z = z)$ would then be defined as:

$$L(z) \equiv \frac{1}{p_0}\int_z^\infty p\left(z'\right)dz' = \frac{1}{p_0}\int_z^\infty \frac{1}{2}p_0\left(1 - \frac{z'}{\sqrt{1+z'^2}}\right)dz' = \frac{1}{2}\int_z^\infty \left(1 - \frac{z'}{\sqrt{1+z'^2}}\right)dz' \tag{2.6}$$

For $z = 0$, $2R$, $4R$ and $6R$, L is $0.5R$, $2.1R$, $4.05R$, and $6.03R$, respectively. That means that for molecular-flow conditions the effective length is approximately the distance between the aperture and the sample.

Calculations for the case of a Knudsen-flow regime, where the mean free path of the molecules is comparable to the aperture size, require numerical simulations (an example can be found in [13]). Analytical expressions exist for the viscous-flow regime where the electron mean free path is much smaller than the aperture size [14]. In this case, the results are molecule specific. For water, the calculations yield an effective length of $1.03R$ after the aperture [11] (i.e. $L(0) = 1.03R$), as compared to $0.5R$ in the case of molecular flow. This is expected since the flow is more directional and pressure is higher on the analyzer axis, along the trajectories of the electrons. In practical terms, the difference of $L(0)$ of $0.53R$ between molecular and viscous-flow regimes is relatively small, i.e. in both cases the effective length is close to the distance of the sample from the aperture. However, for viscous flow the pressure-field gradients near the sample will be complex and dependent on the shape and size of the sample. Recently the pressure field between a planar sample and a differential-pumping aperture was studied using computational fluid dynamics (CFD) simulations in the turbulent-flow regime [15]. The results show that as the pressure in the chamber is increased, the region over which the pressure drop occurs becomes narrower.

The effect of a differential-pumping aperture in front of the sample is that the sample experiences a lower pressure, defined by 2.5 in the molecular-flow regime. A sample $4R$ away from the aperture will experience a pressure of $0.985p_0$ on its surface at the location on the optical axis, which is a sufficiently small difference with respect to the background pressure for most experiments, including experiments using high-vapor pressure samples such as ice at temperatures close to the melting point. $4R$ can thus be considered as the upper limit for the optimal sample-aperture distance. As pointed out earlier, for $p_0 \approx 10$ Torr the effective length (i.e. $\sim 4R$) can only be a few hundred micrometers, requiring aperture diameters of the order of 100 μm or less.

To measure at higher pressures, the effective length has to be made smaller, by positioning the sample closer to the aperture. In this case, the aperture needs to be smaller in order to maintain $\sim p_0$ at the sample surface, and also to limit the gas flow to the first pumping stage. The greatest technical challenge in this situation is to focus the X-ray beam onto the sample area in front of the aperture, without the beam being obstructed by the aperture itself. Synchrotron sources have the advantage that they provide more tightly-focused beams with high flux and smaller divergence, as compared to lab sources. Even in that case, the size and shape of the front aperture have to be engineered carefully to meet the geometrical constraints given by X-ray beam size, divergence, and relative angle with respect to the optical axis of the spectrometer.

The flow of gas through the entrance and subsequent apertures and its effect on the pressure in the various differential-pumping stages can be estimated. In the molecular-flow case, the conductance of an aperture is calculated from the average number of collisions of the gas molecules with the walls, and the area of the aperture:

$$C = JA = \sqrt{\frac{kT}{2\pi m}} A, \tag{2.7}$$

with C as volumetric conductance, A as area of the aperture, k the Boltzmann constant, T the gas temperature, and m as the mass of a molecule of gas. For water vapor passing through a 100-µm aperture at room temperature ($T = 298$ K, $m = 3.0 \times 10^{-26}$ kg, $A = 0.031$ mm^2), the conductance is 5×10^{-3} L/s. As conservation-of-mass equations dictate $C_0 p_0 = C_1 p_1$, for a typical pumping speed of $C_1 \cong 100$ L/s behind the aperture, the pressure ratio between the volumes adjacent to the aperture, p_1/p_0, is 5×10^{-5}. The ratio can be expected to be larger for viscous or Knudsen-flow regimes, but not by much. A typical 4 orders of magnitude pressure drop is routinely attained with the current instruments and apertures of 100-µm diameter. A pressure of ~10 Torr at the sample translates to ~10^{-3} Torr in the first pumping stage, which is about the limit of molecular-flow regime, thus the operating limit of a turbomolecular pump. The apertures that separate the differentially-pumped volumes are typically larger than the first aperture (~few millimeters) and provide ~2 orders of magnitude pressure drop each.

In the preceding paragraphs we have defined a maximum pressure in the sample chamber $\left(p_0^{\max}\right)$ at which APXPS can be performed efficiently. The goal of current technical developments is to increase $p_0^{\max}$ to allow for measurements under more relevant conditions in e.g. heterogeneous catalysis. The following analysis shows that an increase in this maximum sample chamber pressure limit does not lead to higher pressures in the differential pumping stages. The practical electron-scattering limit dictates that the product of the optimal sample-aperture distance and maximum pressure on the sample should be approximately constant, since the optimal sample-aperture distance is proportional to the aperture radius:

$$R p_0^{max} \cong constant \tag{2.8}$$

The pressure in the first pumping stage is proportional to the pressure on the sample and the area of the aperture (i.e. $4\pi R^2$).

$$p_1 \propto R^2 p_0^{max} \tag{2.9}$$

Substituting (2.8) in (2.9) gives:

$$p_1 \propto \frac{\left(R p_0^{max}\right)^2}{p_0^{max}} \tag{2.10}$$

$$p_1 \propto \frac{1}{p_0^{max}} \tag{2.11}$$

This means that a higher maximum sample-chamber-pressure limit does not translate to a higher pressure in the first pumping stage since the effect of the

mandatory decrease in the aperture diameter will outweigh the pressure increase. The same argument may also be used for the latter pumping stages. The flux of the portion of the gas that travels through the first aperture close to the optical axis without being scattered (and thus pumped), eventually reaching the electron-energy analyzer is also proportional to the conductance of the first aperture, thus proportional to R^2. The conclusion is that the pressure limit in current APXPS instruments can be increased as long as the diameter of the first aperture is decreased proportionally.

2.1.2.3 Differentially-Pumped Electrostatic-Lens Systems

The cost of introducing a differential-pumping stage (apart from the financial "cost") is decreasing the collection angle of electrons to a solid angle set by the aperture that subtends the smallest solid angle as seen from the sample (see Fig. 2.3a). Just considering the influence of the first aperture on the detection efficiency, for a sample $4R$ away from the first aperture, the acceptance angle is limited to $2\arctan(R/4R) = 28°$. In the absence of electrostatic lenses, apertures in the latter pumping stages would cut down the acceptance angle dramatically. For example, an aperture of 3 mm diameter, 1 m away from the sample subtends an angle of 0.34°, as compared to the 28° limit of the first aperture, and it would cut down the electron count by almost 4 orders of magnitude. This reduction of electron transmission by a series of apertures in the differentially-pumped lens system was the limiting factor in the first-generation APXPS instruments, all of which were also using laboratory X-ray sources [16, 17].

Fig. 2.3 Schematic illustration of the increase in the electron-collection efficiency with the use of an electrostatic-lens system. An electrostatic-lens system in the first pumping stage is close enough to the sample to collect electrons from a full-angle of ~30°

(a) without electrostatic lens

Electrons

Sample   First aperture   Second aperture

(b) with electrostatic lens

Lens elements
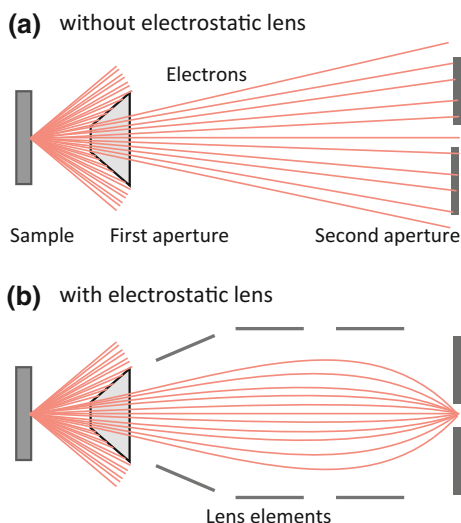
The electrostatic-lens system in an XPS instrument serves several purposes, among them to increase the efficiency with which the electrons are collected from the sample, and it matches the kinetic energy of the electrons to the pass energy of the analyzer. In many recent versions of ambient-pressure XPS instruments, electrostatic lenses are placed in between the differentially-pumped apertures, which increases the acceptance angle markedly, comparable to instruments with conventional electrostatic-lens systems without differential pumping (see Fig. 2.3b).

2.1.2.4 X-ray Sources for Ambient-Pressure XPS

X-ray sources, such as a conventional X-ray tube or a synchrotron, operate under UHV, and for that reason the high vacuum in the X-ray source has to be separated from the ambient pressure in the measurement cell. X-rays are much more weakly absorbed/scattered by matter than electrons. Thus, X-rays can pass through much thicker membranes (i.e. X-ray windows), which separate UHV and high pressure, than electrons. X-rays are also less attenuated by a gas than electrons.

Al, Si and silicon nitride (Si_3N_4) are being used as X-ray-window materials. While thin Al membranes have the highest transmission across the soft X-ray regime, they often develop pinholes and thus vacuum leaks. Si_3N_4 has proven to be the most effective and is the most widespread choice for X-ray windows in APXPS experiments. This is mostly due to the commercially developed, robust, and cheap Si_3N_4 windows. X-ray windows typically have sub-micron thicknesses. Transmission of soft X-rays through Si_3N_4 windows of different thicknesses is shown in Fig. 2.4. It can be seen that typically used, 50–100 nm-thick windows have more than 50% transmission above 300 eV, which is the useful energy range for most XPS experiments. The mechanical stability of Si_3N_4 windows allows for pressure differentials of 1 atm across an active window area of 0.5×0.5 mm^2 for 100 nm-thick membranes.

Fig. 2.4 X-ray transmission through Si_3N_4 windows of different thicknesses [18, 19]
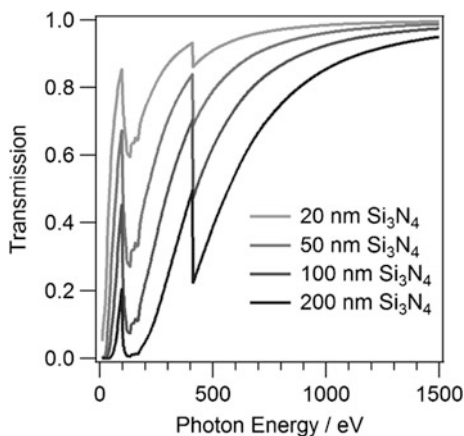
Due to the tight focus and small divergence of X-rays produced by synchrotrons the active X-ray window size can be kept very small in those experiments, which allows the use of thinner membranes (typically 100 nm). For lab-based APXPS experiments monochromatized and focused X-ray sources are preferable (yet much more expensive than unfocused sources), but have a much larger divergence than X-rays originating from a synchrotron source. This requires to either use much larger active window areas or to place the window very close to the sample, which can be problematic due to space constraints in the vicinity of the sample and also the risk of exposing the window to high temperatures during experiments that involve heating the sample. Since laboratory-based X-ray sources in general produce X-rays with energies well in excess of 1 keV, where the transmission of Si_3N_4 is high, thicker and thus larger membranes can be used which can in turn be placed farther away from the sample's surface without cutting into the incident X-ray beam.

2.1.3   Phenomena that Are Relevant to XPS Analysis of Catalysts Under Gas Ambient

2.1.3.1   Monitoring the Gas Phase Over a Solid

When a solid (or liquid) sample is analyzed with APXPS, X-rays not only ionize the sample but also ionize the gas that they traverse. Some part of this ionized gas always falls into the electron-collection volume of the analyzer. This is illustrated in Fig. 2.5a. As a result, peaks of the gas molecules also show up in the XP spectra when the gas partial pressure is above ~0.1 Torr. Photoelectron peaks of gas molecules show up at a few eV higher binding energies than their condensed phase counterparts, and usually don't overlap with them. This constitutes a great way to analyze the gas composition right above the sample simultaneously with the surface composition, and is especially useful when studying molecular transformations, as in the case of catalysis.

As already mentioned, the sample is normally at the same potential as the analyzer (in the case of metals), so their Fermi levels are aligned and a change in the sample's work function does not affect the measured binding energies of electrons from the sample. On the other hand, the reference point of binding energy in gases is the vacuum level. As a result, the observed binding energies from the gas molecules change with the vacuum level of the volume of the gas that is ionized. This is illustrated in Fig. 2.5b where E_{vac}^{gas} is shown to be a linear function of E_{vac}^{sam} (sample) and E_{vac}^{ap} (aperture). Since $E_{vac} = E_F + \Phi$ and all the Fermi levels are aligned, changes in the work function of the sample and the aperture surfaces will cause changes in the observed binding energies for gas molecules.
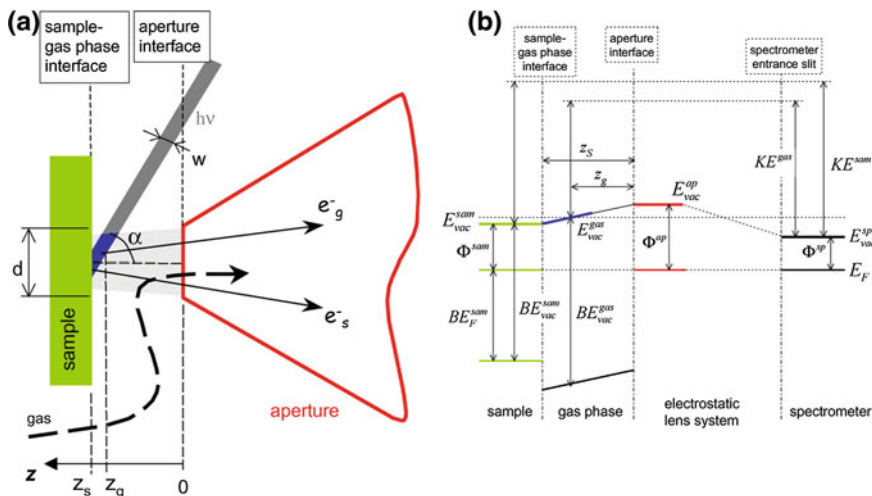
Fig. 2.5 **a** The typical sample/aperture/X-ray beam configuration in an APXPS setup. Part of the gas that is illuminated by the beam is in the acceptance cone of the spectrometer (i.e. blue area). **b** Energy level diagram corresponding to the region in part (**a**). Fermi levels are aligned due to the sample and the whole spectrometer being in electrical contact. The work functions of different parts of the setup are in general different, which results in different vacuum levels. The vacuum level of the gas that is seen by the spectrometer is a function of position, and changes linearly between the sample and the first aperture. Reproduced with permission from [12]

In addition to being affected by the changes in the work functions of the nearby surfaces, putting a bias on the sample (i.e. shifting the Fermi level) will also induce a shift in the gas peaks. This shift will be smaller than the bias applied, and its magnitude will be:

$$\Delta BE_{vac}^{gas} = -\Delta E_{vac}^{gas} = \left(z_g/z_s\right)eV_{bias} \tag{2.12}$$

where e is the magnitude of the electron's charge (positive in sign) and V_{bias} is the voltage applied to the sample. Keep in mind that the change of the binding energies from the sample will be eV_{bias}. This implies that overlapping gas and sample peaks can be separated by applying a high-enough bias to the sample.

In addition to monitoring the gas phase over a solid sample, APXPS can also be used to analyze the gas phase exclusively. Apart from obtaining fundamental electronic-structure information about the molecule, this can provide valuable quantitative information. Intensities from core levels from a material with ideal stoichiometry (such as a gas molecule) can serve as an almost-perfect internal reference. Using such an approach provides a correction factor for the photon flux, and the analyzer transmission function at those kinetic energies. The accuracy of the approach is fundamentally limited by the error that may be introduced by intramolecular electron-scattering effects [20].

A common case for this kind of quantitative analysis is the deconvolution of the O 1s signals of hydroxyls and carbonates on a solid surface, which have almost identical O 1s binding energies. Based on the C 1s and O 1s spectra from a C and O containing gas (e.g. CO_2, CO) as reference, one can calculate an O 1s/C 1s sensitivity factor. Using the C 1s signal of the carbonate and the sensitivity factor, the contribution of the carbonate to the O 1s intensity at the hydroxyl region can be found.

2.1.3.2 Beam Damage

Irradiation by X-rays can cause chemical changes in materials, mostly due to the generation of low-energy (secondary) electrons. The amount of damage depends on the X-ray flux (i.e. photons per area), the energy of the incident X-rays, as well as the chemical composition of the sample. Examples for beam-induced chemical changes are the reduction of oxides and the loss of anions in alkali halides upon irradiation. Conventional anode sources have a relatively low X-ray flux density compared to synchrotron sources and thus beam damage is expected to be slower in the former case. When beam damage takes place on a time scale comparable to that required to measure a spectrum it is easy to check for it by observing changes to the APXPS spectra with time. However, one should always keep in mind that beam damage can happen on a time scale not easily detectable in an XPS experiment (i.e. on a sub-second time scale) which is thus difficult to guard against, unless an independent verification method for the absence of beam damage is available, which to our knowledge has not been implemented so far in an APXPS experiment. Simultaneous IR and APXPS measurements with full spatial overlap might be a route to achieve control over beam damage. Although there are plans for implementing combined vibrational and core-level ambient-pressure spectroscopy experiments in a number of laboratories, a setup that would allow for these measurements has not yet been commissioned.

One way of avoiding beam damage is to continuously prepare a fresh sample surface, as in using a continuous stream of the sample, where the sample is replenished at a rate greater than the rate of beam damage. For a liquid sample, this might be a liquid jet or a droplet train [21–23]; for a solid, a jet of aerosol (solid/gas) or suspension (solid/liquid) [24].

2.1.3.3 Charging

Charging is a major problem in XPS when working with non-conducting samples such as catalysts supported on high band gap materials, e.g. alumina or silica. Charging not only leads to shifting of peaks (in some cases by hundreds of eV) but also to asymmetric broadening in case of inhomogeneous charging. While rigid peak shifts due to homogeneous charging across the whole investigated sample surface can be corrected for by using internal binding-energy standards, asymmetric

broadening makes even relative binding-energy assignments impossible. In UHV, working with charging samples is possible by using an electron flood gun. In this case, low-energy electrons flood the sample and compensate the positive charge accumulated at the sample surface due to the emission of photoelectrons. The flood gun contains a hot emitter and cannot operate above a certain pressure ($\sim 10^{-8}$–10^{-6} Torr depending on the type of emitter). A differentially-pumped flood gun could be the solution but it has not been realized yet.

At a sufficiently high gas pressure in the reaction cell, electrons emitted from the gas molecules hit the sample and partially or completely compensate the charging of the sample. These are mostly secondary electrons but Auger and photoelectrons contribute as well. The extent of compensation depends on many factors such as the chemical composition of the sample/gas, photon flux, photon energy, X-ray incidence angle, and gas pressure. This effect may remove charging completely; but even when it does not the spatial inhomogeneity of the charging may be reduced to an extent that relative binding energies can be measured. In that case a peak with a well-known binding energy can be used as an internal reference to calibrate the binding energy scale.

Figure 2.6 shows the apparent Si 2p binding energy of a muscovite mica sample as a function of water vapor pressure. Muscovite mica is a layered aluminosilicate with intercalated K^+ ions, and its electrical conductivity is similar to aluminas, silicas, or aluminosilicates used as catalysts or catalyst supports. The nominal Si 2p binding energy in mica (~ 102.4 eV), measured in UHV using a flood gun is shown by a horizontal dotted line [12]. The shift of the Si 2p peak in 0.02 Torr water vapor is almost 150 eV, which is not uncommon, and the peak shapes at high charging conditions are quite asymmetric (see the inset spectra in the figure), making interpretation of chemical shifts impossible. As the water vapor pressure is increased from 0.02 to 1.75 Torr, the compensation of charge increases and the apparent binding energy gets closer to its nominal value, not reaching it exactly though. The broadening of the Si 2p peak due to inhomogeneous charging disappears almost completely at 1.75 Torr. In that regard, the increased mobility of K^+ ions under humid conditions, where a thin layer of liquid water forms on the surface, provide another mechanism for distribution of charge uniformly on the surface.

2.1.3.4 Heating and Cooling of Samples

One of the main goals in the field of catalysis research is to find catalysts that perform well at low temperatures, which would decrease the energy costs in industrial processes. Nonetheless catalysis, for the most part, is still a high-temperature science, where below-room-temperature reactions are rare [25]. When it comes to fundamental studies though, temperature may need to be manipulated in either way.
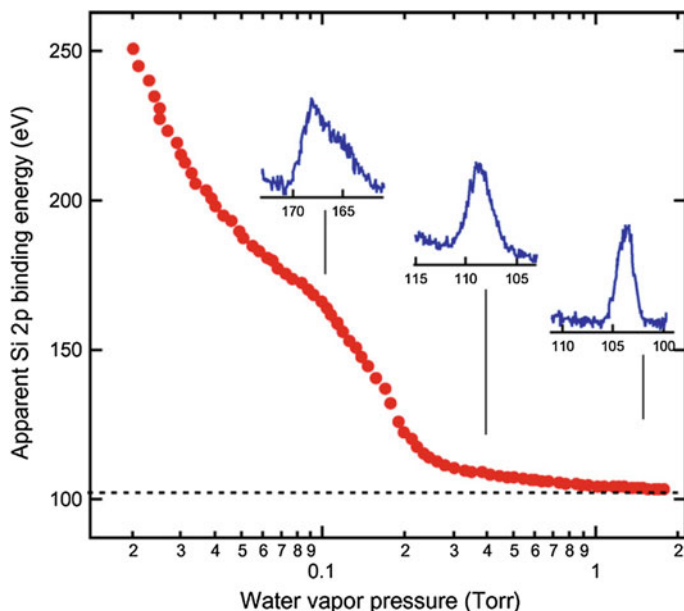
Fig. 2.6 Apparent Si 2p binding energy of a muscovite-mica sample as a function of water vapor pressure. The incident photon energy is 390 eV, with a flux density of 3×10^{11} mm^{-2} s^{-1}. The dotted line indicates the nominal Si 2p BE in muscovite mica. The insets show Si 2p spectra at water vapor pressures of 0.1, 0.4, and 1.7 Torr. Differential charging, which is observed at the lower pressures, is not observed at 1.7 Torr. Reproduced with permission from [12]

Cooling of samples for APXPS experiments constitutes a challenge. Regular schemes used for UHV-type experiments usually form the coldest spot outside the sample, such as on cooling rods, tubes, etc. In that case significant condensation/deposition may take place on these surfaces if the coldest spot has a lower temperature than the condensation point of the gas in the chamber. If the gas is introduced at a smaller rate than the rate of condensation, the pressure in the chamber would be limited by the temperature of the cooling element. In order to prevent such problems, samples can be cooled with Peltier elements, which ensure that the sample is the coldest point in the experimental setup [2].

Heating samples to study catalytic reactions also has some restrictions. Any kind of heating technique that uses a hot filament should use a chemically-resistant filament material, such as Pt. Common materials like W, Ta, and Ir will readily oxidize in oxidizing gases and would be of limited use. However, heating techniques that employ a hot metal such as a Pt filament are inherently problematic if one wants to study a reaction catalyzed also by the heater material. Resistive heaters where the metal is embedded inside a non-reactive ceramic material help overcome this problem.

One example of resistive heating has been applied at the Boreskov Institute in Novosibirsk, Russia [26, 27]. The instrument is a commercial VG-ESCALAB

high-pressure spectrometer. The most recent design of the sample holder uses W wires spot-welded to a single-crystal sample for resistive heating [27]. The small area of the heater wire combined with the relatively inert nature of W surfaces makes the heater applicable for inert or reducing gas atmospheres. A special, pyrolytic boron nitride (PBN)-coated heater produced by Sintec Keramik has also been used in combination with the same instrument [26], allowing the use of oxidizing gases.

Another other instrument that is specially designed for catalysis studies is at the ISISS beamline at BESSY II, in Berlin [28]. That instrument uses an IR laser for heating, with an absorbing contact plate behind the sample. This heating scheme prevents hot spots other than the sample and has been successfully applied for a number of studies involving several different reactions [29–33].

2.1.3.5 Introducing and Analyzing Gases

There are different approaches for introducing gases into an APXPS chamber. The simplest one involves the use of variable leak valves under full, partial, or minimum pumping conditions, pumping being carried out by a turbomolecular pump. Full pumping utilizes the maximum capacity of the turbo pump; thus the pressure in the chamber has to be below $\sim 10^{-3}$ Torr. With a catalyst surface under investigation, this case is similar to a continuous stirred-tank reactor (CSTR) with very high space velocity. At this pressure range, mass transfer by diffusion is faster than the reaction rate and a CSTR approximation is valid. Partial pumping can be achieved by decreasing the conductance to the pump using a valve. Partial pumping increases the pressure in the chamber and decreases the space velocity. The mass-transfer rate decreases due to increased pressure and mass-transfer limitations start becoming significant. Minimum pumping is the case where the chamber is pumped only via the first aperture of the differential-pumping system. Because of the small conductance of the aperture, the space velocity is very small and the system is nearly a batch reactor. The limitation of leak valves is that it is difficult to set exact partial pressures for gases in a gas mixture. This problem can be partially overcome if the gas mixture in the chamber is analyzed by means of a mass spectrometer. It would still not be possible to set the partial pressures precisely but at least to measure them.

The second approach to introducing gas mixtures is using mass flow controllers (MFC). MFCs provide control on the flow rate of each individual gas and thus allow the user to set the desired composition of the inlet gas mixture. The pressure range that one can have using MFCs depends on the flow-rate limits of the MFC and the specifications of the pump used to pump the chamber. Working in the Torr range is possible as well as in high vacuum. MFCs are ideal for experiments in the Torr range with high space velocity.

2.1.3.6 Contamination

Under pressures relevant for APXPS (mTorr to Torr range), a surface site experiences 10^4–10^6 collisions per second. This means even gas impurities with ppm concentration may cover the surface in seconds if the sticking coefficients are not too low. Furthermore, high impingement rates on the chamber walls may also lead to additional impurities. Molecules on the walls may be simply displaced or react with the gas to form new contaminants, eventually ending up on the sample surface. Baseline pressure is not a sufficient indicator of the severity of possible contamination. Even when the baseline pressure is low ($<10^{-9}$ Torr), the walls may have a significant coverage of impurities. The nature of these impurities depends on the history of the chamber.

An example of contamination from a small impurity is Ni carbonyls that form in Ni-containing steel gas lines under high CO pressures and which can decompose on surfaces (especially at high temperatures) to leave metallic Ni. The contamination can be prevented by using Cu tubing and Ni-carbonyl traps. An example for impurities that form due to wall reactions is the formation of elemental halogens by the reaction of oxidizing gases with halide ions on the walls. In our group, we have observed fluorine, chlorine, bromine, and iodine contamination on our samples after introducing NO_2 to our chambers in the mTorr range. O_2 sometimes causes a fluorine contamination which we believe to happen via the same mechanism. Needless to say, this kind of contamination can be prevented only by keeping the chamber walls clean. In certain cases creating a nitrogen plasma in the chamber (followed by a bake-out) may help reduce wall contamination. The best approach to avoid impurities would be to use exchangeable cells, each of which is to be used for one reaction exclusively. Such cells are currently commercially available and are expected to be more widely used for studies in heterogeneous catalysis. Another type of contamination that is relevant at high pressures is the cross contamination that occurs while co-dosing the vapor of a liquid "A" and another gas/vapor "B" that is soluble in that liquid. If the pressure in the chamber and the pressure above liquid A is not high enough, the diffusion rate of B through the dosing valve into vapor/liquid A can be significant. An example is the diffusion of ammonia (NH_3) gas into liquid water during co-dosing. Liquid water can hold as much NH_3 as to end up in the vapor phase for the next experiment. Replacing the contaminated water with fresh water will solve the problem in this case.

2.1.3.7 Reactor Modeling

Industrial reactors may sometimes have limited reaction rates due to mass transfer from the bulk of the reactant stream to the catalyst surface and this fact is always taken into consideration in the reactor's design stage. Catalysis studies under realistic pressures also in general account for this fact. Surface-science studies of model catalysts on the other hand never had to take this into consideration, because the mean free path of molecules at or below high vacuum is larger than the reactor

cell dimensions, and the number of reactant molecules striking the surface is low so that the rate of mixing of gas molecules is always much larger than the rate of reaction. Since APXPS experiments can be performed at pressures where mass transfer becomes an issue, a meaningful interpretation of the data necessitates the understanding of the concentration and temperature gradients in the system.

In an illustrative study, Blomberg et al. reported on real-time monitoring of CO and CO_2 concentrations over a Pd(110) single crystal during catalytic CO oxidation [34]. Their experimental chamber and the CO concentration map (obtained by laser-induced fluorescence) over the Pd(110) surface at nearly steady-state is shown in Fig. 2.7. The reaction was carried out under flow conditions (space velocity: $\sim 1 \ s^{-1}$) at 80 Torr total pressure and a $CO:O_2:Ar$ reactant mixture of 1:1:2 ratio. The concentration map for CO shows a CO-depleted region above the Pd(110) surface. This region extends ~ 5 mm in every direction from the surface.

The conditions in APXPS experiments are usually different from the conditions studied by Blomberg et al. in the sense that flow rates of gases are smaller and the pressures involved are typically 2-3 orders of magnitude lower. In addition, the presence of the nozzle near the sample affects the concentration gradients.

One of the tools to incorporate mass (and heat) transfer effects into the analysis of APXPS data is multiscale modeling of experimental chambers. An example of this, although not an APXPS setup, is the modeling of the chamber shown in Fig. 2.7a [35]. In that work, Matera et al. show that it is possible to extract information about the state of the catalyst surface by combining Monte Carlo simulations (energies computed with DFT) and computational fluid dynamics. Including similar simulations to APXPS experiments in the future can surely contribute to data interpretation.
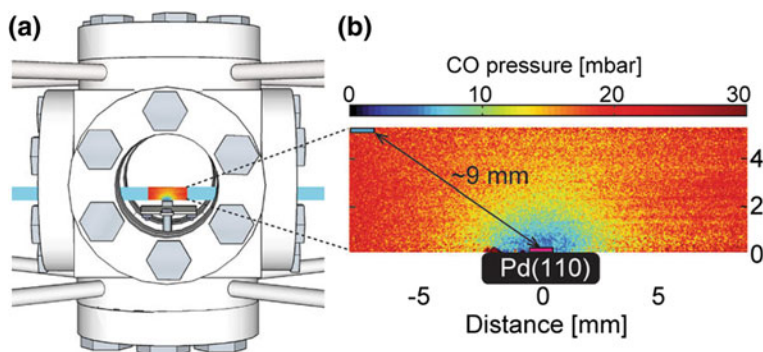
Fig. 2.7 Monitoring the concentration gradient in the gas phase during CO oxidation over a Pd (110) crystal. The total pressure is 80 Torr, with a $CO:O_2:Ar$ ratio of 1:1:2. **a** Reactor setup showing the sample and the laser sheet used to monitor the CO concentration with 2D spatial resolution. **b** The CO partial pressure map above the sample measured via laser-induced fluorescence. Reproduced from [34] under the "Standard ACS Author Choice/Editors' Choice Usage Agreement"

2.2 Examples

2.2.1 CO Oxidation on Ru

There has been a hot debate about the active phase(s) of Ru catalysts in the CO oxidation reaction [36–38]. It was known for a long time that the Ru(0001) surface is inactive for CO oxidation under UHV conditions [39–41], however, it is remarkably active in the Torr pressure range [42, 43]. Under these conditions, Goodman and Peden proposed a O-(1 × 1) structure on Ru(0001) (~1ML of O), whereas Over and co-workers argued for a RuO_2(110) surface, which forms under reaction conditions as the catalytically-active phase. Several ex situ, in situ, and *operando* techniques have been used to address the question. APXPS was used to investigate the reaction on Ru(0001) [44] and Ru(10–10) [45] single crystals, nanoparticles [46], and thin films [47]. The current understanding about this system is that even a poorly-ordered oxide layer (1–3 ML of oxygen) on Ru metal is active in CO oxidation, i.e. an ordered surface such as RuO_2(110) is not necessary [48].

Blume et al. studied CO oxidation under different CO/O_2 ratios over a pressure range of 10^{-4}–10^{-1} Torr [44]. The sample was a Ru(0001) single crystal, which showed different oxides as a function of reaction conditions. The reaction product (CO_2) was monitored using a mass spectrometer that was mounted at the first differential-pumping stage of the electron spectrometer. O 1s and Ru $3d_{5/2}$ spectra were monitored in a 0.075 Torr, 1:1 $CO:O_2$ mixture, while the temperature was increased at a constant rate. Changes in the O 1s spectrum indicated a transition at ~500 K from a surface oxide, where the top few layers are incorporated with ~1–3 ML of O atoms, to a rutile-RuO_2 phase, which is expected to have the RuO_2(110) orientation [49]. This transition, however, did not correspond to a change in the CO_2 production rate. It was concluded that "there was no distinct difference in catalytic activity between the stoichiometric RuO_2(110) and a few-layers-thick, poorly-ordered surface oxide".

Toyoshima and coworkers studied CO oxidation on Ru(10–10) [45]. The reaction was carried out in a 0.11 Torr gas mixture with 1:10 $CO:O_2$ ratio, under flow conditions, at temperatures ranging from 390 to 570 K. The formation of CO_2 was monitored using a mass spectrometer installed at the differential-pumping system of the electron spectrometer. Transformation of the surface around 460 K from a chemisorbed oxygen state to a ~ 1 nm thick RuO_2 layer (equivalent to 4–5 atomic layers) was observed with APXPS. At the temperatures investigated, oxide growth is kinetically limited. RuO_2 is expected to have the (100) orientation [50]. The transformation was correlated with an increase in reaction rate, observed by an increase in CO_2 mass signal, and it was concluded that the thin RuO_2 layer was the catalytically active phase for the reaction.

Qadir et al. studied the surface structure of Ru catalysts under CO, O_2, and a CO + O_2 mixture (0.08 Torr CO + 0.2 Torr O_2) [46, 47]. The difference in catalytic activity of 2.8 and 6 nm-sized Ru nanoparticles, which had been reporter earlier [51], was attributed to the different thicknesses of the oxide layers that grew

on the nanoparticles under reaction conditions [46]. Particles having a 2.8 nm diameter grew a thicker oxide layer than those of 6 nm diameter, which in turn suppressed the catalytic activity. The same type of deactivation behavior was also observed for Ru in the form of a thin film [47]. Thin-film Ru formed a thicker oxide under oxidizing conditions and this oxide layer was more difficult to reduce than the oxide layers that formed on nanoparticles.

2.2.2   CO Oxidation on Pd

Unlike Ru, metallic surfaces of Pd, Pt, and Rh are very active for CO oxidation. While the metallic surface is probably the most active state in CO oxidation [39, 52, 53], APXPS studies showed that surface oxides that form on these metals under reaction conditions may have significant activity too.

Blomberg et al. studied CO oxidation over Pd(100) using APXPS, up to a total pressure of 1 Torr, with 1:1 and 1:4 $CO:O_2$ ratios and over a temperature range of 420–680 K [54]. In a 1:1 $CO:O_2$ gas ambient, they observed the transformation of a CO-poisoned surface to an oxygen-covered metallic surface at increasing temperatures with increasing total pressure (e.g. 523 K for 0.01 Torr and 608 K for 0.5 Torr). The transformation was concomitant with the depletion of CO and the emergence of CO_2 in the gas-phase spectra, which implied that the new surface was catalytically active. Up to a total pressure of 0.5 Torr, the oxygen coverage of the active surface was below 0.4 ML, which is the range consistent with $p(2 \times 2)$ or $c(2 \times 2)$-overlayer structures. At a total pressure of 1 Torr, the oxygen coverage of the active surface increased significantly to 0.75 ML, consistent with a (5×5) oxidic-precursor structure observed earlier [55]. This increase in O coverage with pressure was interpreted as a sign of the pressure gap for this system existing somewhere above 1 Torr. With the use of a more oxidizing (1:4) $CO:O_2$ mixture at 0.5 Torr the authors observed the formation of a yet higher O coverage of 0.8 ML, which was interpreted as a $\sqrt{5} \times \sqrt{5} - R27$ surface-oxide phase [55, 56].

In a series of experiments Kondoh and co-workers studied CO oxidation over Pd (111), Pd(100), and Pd(110) [57–60]. Reaction products were monitored using a mass spectrometer placed at one of the differential-pumping stages. They used a $CO:O_2$ ratio of 1:10 (much more oxidizing than used by Blomberg et al.) with a total pressure of 0.22 Torr. Typical CO-poisoning behavior was observed at low temperatures (below 473 K, 463 K, and 438 K for Pd(111), Pd(100), and Pd(110), respectively), consistent with literature data. The use of an oxidizing gas mixture resulted in the formation of a $\sqrt{5} \times \sqrt{5}$ surface oxide on Pd(100) under reaction conditions (i.e. ~473 K). Figure 2.8 shows the CO_2 signal from the mass spectrometer as a function of the Pd(100) temperature, and Pd $3d_{5/2}$/C 1s spectra at certain points during heating, labeled A-D. Spectrum "E" corresponds to a bulk-oxide surface, which was not observed under reaction conditions but only under pure O_2 flow. The CO-poisoned region (A–B), the activation region (B–C),

and the active region (C–D) can be seen from the CO_2 mass spectrometer signal in Fig. 2.8a. The activity of the surface oxide and the surface-oxygen content decrease with increasing temperature between points C and D. The authors concluded that an active oxygen species (i.e. "the up-side O" in the $\sqrt{5}$ surface oxide) was being lost at higher temperatures due to decomposition.

In CO-oxidation experiments using *operando* techniques such as APXPS, the emergence of a surface phase (such as an oxide) at the onset of catalytic activity is usually regarded as proof that this phase is responsible for the change in activity. Recent work by Matera et al. shows that this may not be the case for the well-studied Pd(100) surface [35]. By multiscale modeling of a catalytic reactor, they show that metallic Pd(100), which is a minority phase under the given CO-oxidation conditions, may be responsible for most of the observed activity. This work is a reminder that the activity of possible minority phases, which may not be quantified by XPS, can be responsible for the most, if not all, of the catalytic activity.

Fig. 2.8 CO oxidation on Pd (100) investigated by APXPS and mass spectrometry (MS). **a** CO_2 MS signal as a function of sample temperature under 2×10^{-1} Torr O_2 and 2×10^{-2} Torr CO. XP spectra are shown at points A–D. **b**, **c** Pd $3d_{5/2}$ and C 1s spectra, respectively, at points A–D and E. Spectra "E" were taken at 643 K, under 2×10^{-1} Torr pure O_2, after CO dosing was stopped. Adapted with permission from [58]. Copyright 2015 American Chemical Society
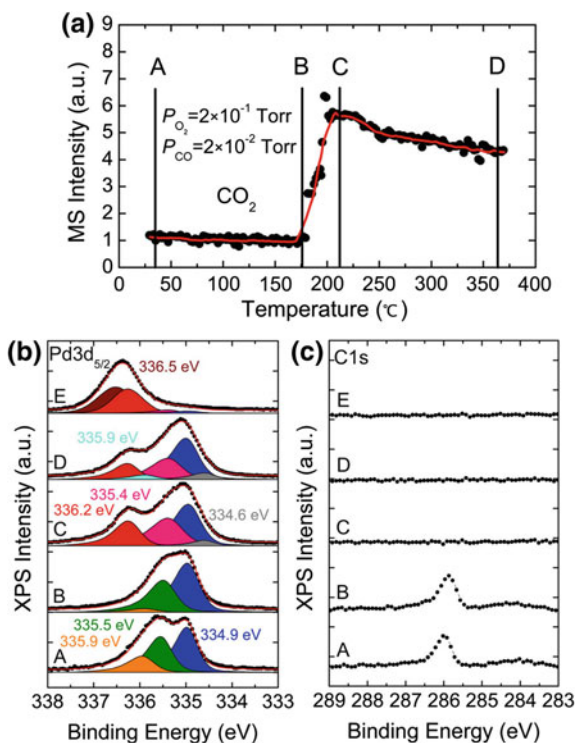
2.2.3 Catalytic Oxidation of Small Organic Molecules

Gabasch et al. studied the oxidation of CH_4 on the Pd(111) surface. A 1:5 reaction mixture of CH_4/O_2 was used at a pressure of 0.25 Torr [61]. The reaction products were monitored using two mass spectrometers, one in the first differential-pumping stage, and the other connected directly to the chamber via an adjustable capillary leak. The reaction shows a well-known activity hysteresis for the (111) surface as a function of temperature. The study looked into this effect by monitoring the surface composition and structure during reaction, both during heating and cooling. A detailed analysis involving rigorous peak fitting was used to identify the different oxygen species at the Pd(111) surface [62, 63]. It was observed that during heating, in the 530–650 K range, PdO seeds form on the 2D Pd_5O_4 surface oxide. The combination of these two oxides has a high catalytic activity, which translates into increased CO_2 and H_2O production during heating of the sample. During cooling, the increased catalytic activity was not observed, and neither was the Pd_5O_4 + PdO seed mixture. The surface oxide present during cooling had even less O than Pd_5O_4. The absence of PdO seed formation during cooling was explained on the basis of kinetic limitations to oxygen supersaturation, which is probably needed for the nucleation of the PdO seeds.

Kaichev et al. used APXPS to determine the formation mechanism of self-sustained oscillations that are observed during partial oxidation of propane over Ni foil [64]. The oscillations were monitored via the quantitative chemical analysis of the gas mixture using mass spectrometry and gas chromatography. The total pressure in the chamber was constant at 0.38 Torr. When the propane-to-oxygen ratio was varied, oscillations were observed for ratios of 3:1–15:1 (propane:oxygen) and over a temperature range of 873–973 K. Each period of the oscillation is divided into two regions, an active and an inactive half-period. The active region is typically shorter than the inactive region (see Fig. 2.9) and the ratio of the catalytic activity between the active and inactive period is around 40. The authors observed that the Ni 2p spectrum is typical of NiO during the inactive period and metallic Ni during the active period. O 1s spectra corroborate this finding while also showing a small amount of surface oxygen (0.2–0.4 ML) on metallic Ni. The sample temperature and mass spectrometer signals of CO, H_2, O_2, and H_2O as a function of time are shown in Fig. 2.9, together with Ni 2p and O 1s spectra before, during, and after the active half-period. The thickness of the oxide layer during the inactive half-period is estimated to be at least 3 nm. The authors of this study conclude that the reaction proceeds via a Langmuir–Hinshelwood mechanism on the metallic surface whereas a Mars–van Krevelen mechanism is at play when the oxide is present. This work illustrates the importance of in situ studies since these oscillations are very difficult or impossible to study using ex situ measurements.

Another example of APXPS studies in heterogeneous catalysis is the investigation of the selectivity of Ag-based catalysts for the ethylene-epoxidation reaction, which was studied by Rocha et al. [65], specifically the effect of Cl as a promoter. The sample was a commercial Ag nanopowder (<100 nm) pressed into a pellet.
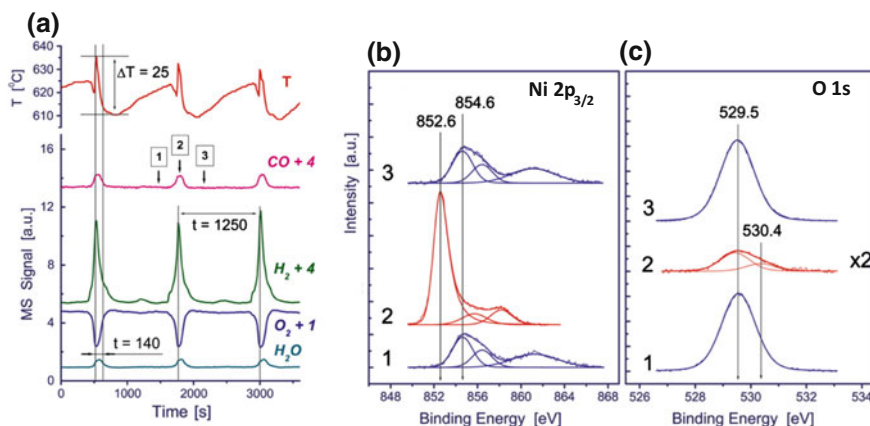
Fig. 2.9 Example for monitoring the oscillatory surface state of a catalyst surface (Ni foil) during partial oxidation of propane at 0.38 Torr with a propane:oxygen ratio of 8:1. **a** Catalyst temperature and MS signals of CO, H_2, O_2, and H_2O as a function of time (The MS signals from H_2, CO, and O_2 are vertically shifted by the factor shown in the legends). **b**, **c** Ni 2p and O 1s spectra before (*1*), during (*2*), and after (*3*) the short reactive half-period, respectively. Reproduced with permission from [64]

The chamber was kept at 0.23 Torr fixed pressure. An oxygen-rich feed with 1:2 C_2H_4:O_2 ratio was used with a flow rate of 4 mL/min. The gases were introduced using mass flow controllers. The sample temperature was fixed at 503 K using an infrared laser and a PID feedback. Gas chromatography was used to quantify the product concentrations and selectivity.

The analysis of the different oxygen species on Ag using APXPS is complex, and has been done thoroughly in earlier studies [66, 67]. Based on these references, the authors grouped different O 1s peaks under three categories: nucleophilic oxygen, electrophilic oxygen, and contamination (see Fig. 2.10b). The binding energies of the O 1s peaks increase in the same order. The electrophilic-to-nucleophilic oxygen ratio (O_{elec}/O_{nucl}) was used as a descriptor of the surface. During a 12-hour run on stream with an un-promoted sample, this ratio changes slowly over time and it correlates positively with the selectivity of the catalyst.

The results of the chlorine-promotion experiments are shown in Fig. 2.10. After more than 14 h on stream, Cl was added to the system by pulsing ethyl chloride (diluted in He) into the inlet stream (Fig. 2.10a). The surface of the Ag catalyst chlorinated immediately, as observed from the increase in the Cl 2p intensity (Fig. 2.10c). The selectivity of the catalyst increased, mostly due to a decrease in the CO_2 production (i.e. suppression of the combustion reaction). Introducing more Cl to the system with two more pulses resulted in more Cl on the surface and a further increase in selectivity. The correlation of O_{elec}/O_{nucl} ratio and ethylene oxide selectivity with chlorine content on the surface is clear (Fig. 2.10d). The increase in surface-Cl concentration resulted in a decrease of nucleophilic oxygen on the surface and concomitant decrease of the CO_2 production rate, whereas the amount
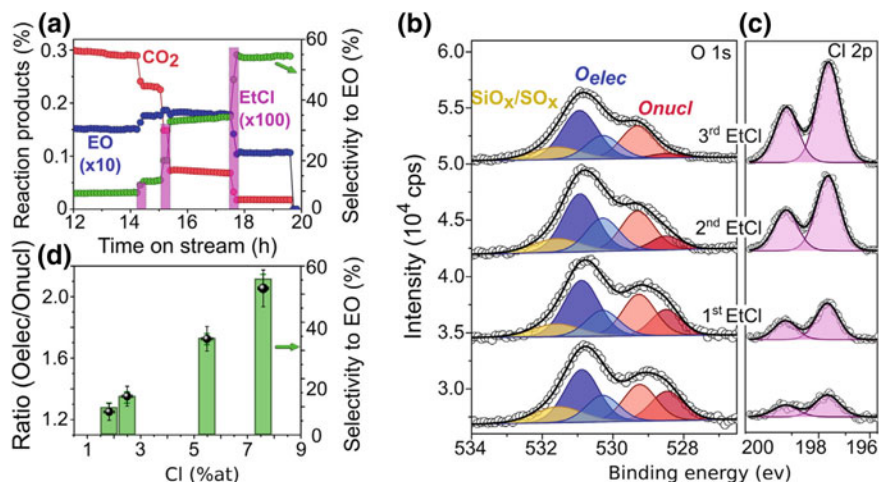
Fig. 2.10 Ethylene-epoxidation reaction studied using APXPS. **a** CO_2, ethylene oxide, and ethyl chloride concentrations in the chamber, and ethylene oxide selectivity as a function of time. **b**, **c** O 1s and Cl 2p spectra before and after ethyl chloride pulses. **d** correlation of O_{elec}/O_{nucl}, ethylene oxide selectivity, and chlorine concentration on the surface. Reproduced with permission from [66]

of electrophilic oxygen and the ethylene oxide production rate increased with the first two pulses but decreased on the third one. The total oxygen content of the surface and ethylene conversion also decreased after the third pulse. The results indicate that Cl promotes the selectivity via a site-blocking mechanism by mainly suppressing the combustion reaction through the removal of nucleophilic oxygen species from the surface. The increase in the concentration of electrophilic oxygen species was rather limited, but the increase in the ethylene oxide production rate was quantifiable. Excess Cl was detrimental for the activity of the catalyst.

2.3 Summary

We have discussed some of the main challenges for the use of XPS to *operando* studies of heterogeneous catalysts, and how they can be addressed using ambient-pressure XPS. The fundamental limit for increasing the pressure in APXPS studies is the scattering of electrons in the gas on their way from the sample surface to the entrance aperture of the differentially-pumped electron spectrometer. Currently, the pressures that one can work routinely is on the order of 10–20 Torr for water vapor, and less than that for molecules with stronger scattering cross sections, i.e. most gases. Expanding the pressure limit to more realistic conditions close to and above one atmosphere is a technical challenge that will most likely be overcome in the near future. Working at higher electron kinetic energies will be beneficial (although

reducing the surface sensitivity). APXPS at higher electron kinetic energies (up to 10 keV) can enable the study of microporous and mesoporous catalysts like zeolites with higher sensitivity to the inner surfaces (e.g. pores) of realistic catalytic materials. The main avenue for increasing the pressure limit in APXPS is the reduction in entrance aperture size, which allows to reduce the path length of the electrons through the gas proportionally. Working at higher pressures will also help reduce charging of insulating samples, but at the same time mass-transfer effects have to be taken into account, in particular differences in the composition of the gas in the background of the chamber, the mass spectrometer, and the gas right above the surface. Modeling of fluid flow and concentration gradients will thus be an important part of data analysis for measurements at more realistic pressures.

References

1. A. Jablonski, C.J. Powell, J. Electron. Spectrosc. **199**, 27 (2015)
2. D.F. Ogletree, H. Bluhm, E.D. Hebenstreit, M. Salmeron, Nucl. Instrum. Methods A. **601**, 151 (2009)
3. S. Tanuma, C.J. Powell, D.R. Penn, Surf. Interface Anal. **21**, 165 (1994)
4. A. Kolmakov, D.A. Dikin, L.J. Cote, J.X. Huang, M.K. Abyaneh, M. Amati, L. Gregoratti, S. Gunther, M. Kiskinova, Nat. Nanotechnol. **6**, 651 (2011)
5. J. Kraus, R. Reichelt, S. Gunther, L. Gregoratti, M. Amati, M. Kiskinova, A. Yulaev, I. Vlassiouk, A. Kolmakov, Nanoscale **6**, 14394 (2014)
6. J.J. Velasco-Velez et al., Angew. Chem. Int. Ed. **54**, 14554 (2015)
7. C.H. Wu, R.S. Weatherup, M.B. Salmeron, Phys. Chem. Chem. Phys. **17**, 30229 (2015)
8. J.J. Velasco-Velez et al., Rev. Sci. Instrum. **87**, 53121 (2016)
9. R.S. Weatherup, B. Eren, Y. Hao, H. Bluhm, M.B. Salmeron, J. Phys. Chem. Lett. **7**, 1622 (2016)
10. M. Salmeron, R. Schlogl, Surf. Sci. Rep. **63**, 169 (2008)
11. D.F. Ogletree, H. Bluhm, G. Lebedev, C.S. Fadley, Z. Hussain, M. Salmeron, Rev. Sci. Instrum. **73**, 3872 (2002)
12. H. Bluhm, J. Electron. Spectrosc. **177**, 71 (2010)
13. M.E. Grass, P.G. Karlsson, F. Aksoy, M. Lundqvist, B. Wannberg, B. S. Mun, Z. Hussain, and Z. Liu, Rev. Sci. Instrum. **81** (2010)
14. D.R. Miller, in *Atomic and molecular beam methods*, ed. by G. Scoles (Oxford University Press, New York, 1988), p. 14
15. J.M. Kahk et al., J. Electron. Spectrosc. **205**, 57 (2015)
16. H. Siegbahn, K. Siegbahn, J. Electron. Spectrosc. Relat. Phenom. **2**, 319 (1973)
17. H. Siegbahn, J. Phys. Chem. **89**, 897 (1985)
18. B.L. Henke, E.M. Gullikson, J.C. Davis, Atom. Data Nucl. Data **54**, 181 (1993)
19. X-Ray Interactions With Matter, http://henke.lbl.gov/optical_constants/. Accessed 15 Jul 2015)
20. J. Soderstrom et al., Phys. Rev. Lett. **108** (2012)
21. D.E. Starr, E.K. Wong, D.R. Worsnop, K.R. Wilson, H. Bluhm, Phys. Chem. Chem. Phys. **10**, 3093 (2008)

22. M.A. Brown, R. D'Auria, I.F.W. Kuo, M.J. Krisch, D.E. Starr, H. Bluhm, D.J. Tobias, J.C. Hemminger, Phys. Chem. Chem. Phys. **10**, 4778 (2008)
23. M. Faubel, B. Steiner, J.P. Toennies, J. Chem. Phys. **106**, 9013 (1997)
24. M.A. Brown, I. Jordan, A.B. Redondo, A. Kleibert, H.J. Woerner, J.A. van Bokhoven, Surf. Sci. **610**, 1 (2013)
25. U. Dingerdissen, A. Martin, D. Herein, H.J. Wernicke, in *Handbook of Heterogeneous Catalysis* (Wiley-VCH Verlag GmbH & Co. KGaA, 2008)
26. V.I. Bukhtiyarov, V.V. Kaichev, I.P. Prosvirin, Top. Catal. **32**, 3 (2005)
27. A. Knop-Gericke et al., Adv. Catal. **52**, 213 (2009)
28. ISISS Station at BESSY II, https://www.helmholtz-berlin.de/pubbin/igama_output?modus= einzel&gid=1671. Accessed 28 Jul 2015
29. V.I. Bukhtiyarov, A.I. Nizovskii, H. Bluhm, M. Havecker, E. Kleimenov, A. Knop-Gericke, R. Schlogl, J. Catal. **238**, 260 (2006)
30. E. Kleimenov et al., Surf. Sci. **575**, 181 (2005)
31. D. Teschner et al., J. Catal. **242**, 26 (2006)
32. E. de Smit, F.M.F. de Groot, R. Blume, M. Havecker, A. Knop-Gericke, B.M. Weckhuysen, Phys. Chem. Chem. Phys. **12**, 667 (2010)
33. C. Rameshan et al., J. Catal. **276**, 101 (2010)
34. S. Blomberg, C. Brackmann, J. Gustafson, M. Alden, E. Lundgren, J. Zetterberg, ACS Catal. **5**, 2028 (2015)
35. S. Matera, S. Blomberg, M.J. Hoffmann, J. Zetterberg, J. Gustafson, E. Lundgren, K. Reuter, ACS Catal. **5**, 4514 (2015)
36. D.W. Goodman, C.H.F. Peden, M.S. Chen, Surf. Sci. **601**, 5663 (2007)
37. D.W. Goodman, C.H.F. Peden, M.S. Chen, Surf. Sci. **601**, L124 (2007)
38. H. Over, M. Muhler, A.P. Seitsonen, Surf. Sci. **601**, 5659 (2007)
39. T. Engel, G. Ertl, in *Advances in Catalysis*, edited by H. P. D.D. Eley, B.W. Paul (Academic Press, 1979), p. 1
40. H.I. Lee, J.M. White, J. Catal. **63**, 261 (1980)
41. V.I. Savchenko, G.K. Boreskov, A.V. Kalinkin, A.N. Salanov, Kinet Catal+ **24**, 983 (1983)
42. N.W. Cant, P.C. Hicks, B.S. Lennon, J. Catal. **54**, 372 (1978)
43. C.H.F. Peden, D.W. Goodman, J. Phys. Chem-us **90**, 1360 (1986)
44. R. Blume et al., J. Catal. **239**, 354 (2006)
45. R. Toyoshima, M. Shimura, M. Yoshida, Y. Monya, K. Suzuki, K. Amemiya, K. Mase, B.S. Mun, H. Kondoh, Surf. Sci. **621**, 128 (2014)
46. K. Qadir, S.H. Joo, B.S. Mun, D.R. Butcher, J.R. Renzas, F. Aksoy, Z. Liu, G.A. Somorjai, J. Y. Park, Nano Lett. **12**, 5761 (2012)
47. K. Qadir, S.M. Kim, H. Seo, B.S. Mun, F.A. Akgul, Z. Liu, J.Y. Park, J. Phys. Chem. C **117**, 13108 (2013)
48. H. Over, Chem. Rev. **112**, 3356 (2012)
49. H. Over, Y.D. Kim, A.P. Seitsonen, S. Wendt, E. Lundgren, M. Schmid, P. Varga, A. Morgante, G. Ertl, Science **287**, 1474 (2000)
50. Y.D. Kim, S. Schwegmann, A.P. Seitsonen, H. Over, J. Phys. Chem. B **105**, 2205 (2001)
51. S.H. Joo, J.Y. Park, J.R. Renzas, D.R. Butcher, W.Y. Huang, G.A. Somorjai, Nano Lett. **10**, 2709 (2010)
52. F. Gao, Y.L. Wang, D.W. Goodman, J. Phys. Chem. C **114**, 6874 (2010)
53. T. Engel, G. Ertl, J Chem Phys **69**, 1267 (1978)
54. S. Blomberg et al., Phys. Rev. Lett. **110** (2013)
55. M. Todorova et al., Surf. Sci. **541**, 101 (2003)
56. P. Kostelník, N. Seriani, G. Kresse, A. Mikkelsen, E. Lundgren, V. Blum, T. Šikola, P. Varga, M. Schmid, Surf. Sci. **601**, 1574 (2007)
57. R. Toyoshima et al., J. Phys. Chem. C **116**, 18691 (2012)
58. R. Toyoshima, M. Yoshida, Y. Monya, K. Suzuki, B.S. Mun, K. Amemiya, K. Mase, H. Kondoh, J. Phys. Chem. Lett. **3**, 3182 (2012)

59. R. Toyoshima, M. Yoshida, Y. Monya, K. Suzuki, K. Amemiya, K. Mase, B.S. Mun, H. Kondoh, J. Phys. Chem. C **117**, 20617 (2013)
60. H. Kondoh, R. Toyoshima, Y. Monya, M. Yoshida, K. Mase, K. Amemiya, B.S. Mun, Catal. Today (2015)
61. H. Gabasch et al., J. Phys. Chem. C **111**, 7957 (2007)
62. H. Gabasch et al., Surf. Sci. **600**, 2980 (2006)
63. D. Zemlyanov et al., Surf. Sci. **600**, 983 (2006)
64. V.V. Kaichev, A.Y. Gladky, I.P. Prosvirin, A.A. Saraev, M. Hävecker, A. Knop-Gericke, R. Schlögl, V.I. Bukhtiyarov, Surf. Sci. **609**, 113 (2013)
65. T.C.R. Rocha, M. Havecker, A. Knop-Gericke, R. Schlogl, J. Catal. **312**, 12 (2014)
66. V.I. Bukhtiyarov, M. Havecker, V.V. Kaichev, A. Knop-Gericke, R.W. Mayer, R. Schlogl, Phys. Rev. B **67** (2003)
67. T.C.R. Rocha, A. Oestereich, D.V. Demidov, M. Havecker, S. Zafeiratos, G. Weinberg, V.I. Bukhtiyarov, A. Knop-Gericke, R. Schlogl, Phys. Chem. Chem. Phys. **14**, 4554 (2012)